Journal of Advanced Ceramics

Volume 6 | Issue 4 Article 3

2017

Prediction of tensile power law creep constants from compression and bend data for ZrB_2-20 vol% SiC composites at 1800 °C

Ali KHADIMALLAH
Department of Mechanical Engineering, University of Houston, Houston, TX, USA

Marc W. BIRD
Department of Mechanical Engineering, University of Houston, Houston, TX, USA

Kenneth W. WHITE
Department of Mechanical Engineering, University of Houston, Houston, TX, USA

Journal of Advanced Ceramics
2017, **6**(4): 304–311
https://doi.org/10.1007/s40145-017-0242-4
ISSN 2226-4108
CN 10-1154/TQ

Research Article

Prediction of tensile power law creep constants from compression and bend data for ZrB_2–20 vol% SiC composites at 1800 ℃

Ali KHADIMALLAH*, Marc W. BIRD, Kenneth W. WHITE

Department of Mechanical Engineering, *University of Houston*, *Houston*, *TX*, *USA*

Received: January 12, 2017; Revised: July 31, 2017; Accepted: August 22, 2017

Abstract: Here we consider our four-point flexure and compression creep results obtained under Ar protection at 1800 ℃ to predict the tensile creep behavior of a ZrB_2–20 vol% SiC ultra-high temperature ceramic. Assuming power law creep, and based on four-point bend data, we estimated the uniaxial creep parameters using an analytical method present in the literature. Both predicted and experimental compressive stress exponents were found to be in excellent agreement, 1.85 and 1.76 respectively, while observation of the microstructure suggested a combination of diffusion and grain boundary sliding creep mechanisms in compression. Along with the microstructural evidence associated with the tensile regions of the flexure specimens, the predicted tensile stress exponent of 2.61 exceeds the measured flexural value of 2.2. We assert an increasing role of cavitation to the creep strain in pure tension. This cavitation component adds to the dominant grain boundary sliding mechanism as described below and elsewhere for flexural creep.

Keywords: power law creep parameters; four-point flexure; compression; tension; creep mechanisms

1 Introduction

Ultra-high temperature ceramics (UHTCs), namely ZrB_2 and HfB_2, are designed to operate at temperatures as high as 2400 ℃ due to their high melting points, oxidation resistance, and mechanical properties [1–6]. Improved oxidation behavior as well as enhanced fracture strength and toughness can be achieved by addition of 20–30 vol% of SiC [2,7]. Creep behavior of these materials is particularly important for several applications such as re-entry vehicles and hypersonic aircraft, which involve exposure to high temperatures for extended periods of time [4,8]. In general, characterizing the creep behavior of materials requires the determination of the strain rate–stress relationship which usually exhibits three different regions, namely primary, secondary, and ternary. Secondary creep is a steady-state stage where, tensorially, the strain rate components take the following form:

$$\dot{\varepsilon}_{ij} = \dot{\varepsilon}_0 \left(\frac{\sigma_e}{\sigma_0} \right)^n \frac{3}{2} \frac{S_{ij}}{\sigma_e} \tag{1}$$

where ε_0 and σ_0 are reference strain and stress states, respectively. σ_e is the Von Mises stress corresponding to the deviatoric stress tensor S_{ij}, and n is the stress exponent. Under pure uniaxial deformation configuration, the steady-state-strain rate $\dot{\varepsilon}_s$ reduces to [9]:

$$\dot{\varepsilon}_s = A\sigma^n \tag{2}$$

where the pre-exponent constant A accounts for temperature and microstructural effects, and the stress exponent n depends on the relevant rate-limiting mechanism.

* Corresponding author.
E-mail: akhadimallah@uh.edu

Creep in tension and compression are often induced by different deformation mechanisms. For example, silicon nitride was subjected to compressive and tensile creep stresses ranging between 10 and 300 MPa at temperatures between 1350 and 1400 ℃ [10]. Over the entire stress range, compressive creep rates showed a linear dependence with stress. Creep rate in tension, on the other hand, followed an exponential trend at high stresses. Observation of the microstructure showed that, unlike compression, creep in tension is controlled by cavity formation. At 1.8% strain, the volume fraction of cavities in compression was only 18% of that in tension [10]. In general, polycrystalline materials with a viscous grain boundary phase exhibit larger creep strains in tension compared to compression [11]. The aforementioned example of silicon nitride shows how different creep in tension and compression can be. Thus, tensile and compressive components of creep must be separately studied to completely discern the associated deformation mechanisms. However, reliable data from high temperature unidirectional tests are not always straightforward. In fact, buckling, gripping, and fixture-related issues, usually encountered during these tests, hinder the collected data. In this context, many attempts were made to extract the tensile and compressive components from bend data since (1) bending tests are easier to conduct and (2) bending deformation can be seen as a combination of tension and compression. A first separation of individual tensile and compressive components from bend data was done by Finnie [12]. In his analysis, Finnie extracted the power law creep parameters for a trapezoidal cross-sectional specimen assuming a linear dependence between strains and stresses, i.e., $n_c = n_t = 1$ and $A_c \neq A_t$ in Eq. (2), where the subscripts c and t refer to compression and tension respectively. Such assumption presumes identical behaviors in tension and compression and prior knowledge of the considered material. Talty and Dirks [13] extended the work done by Finnie on the same specimen geometry while $A_c \neq A_t$ and $n_c = n_t = N$, with N an arbitrary number. They obtained excellent agreement with silicon nitride four-point bending results where a common stress exponent of 2 was determined for compression and tension. Xu *et al.* [14] proposed an analytical solution correlating the creep parameters to the load point deflection and the applied load in a three-point bending configuration. A parametric finite element analysis was conducted showing the parameter correlations. Chuang [15] investigated non-symmetric creep behavior where compression and tension were assumed to have completely independent behaviors (i.e., $n_c \neq n_t$ and $A_c \neq A_t$). Two governing equations relating the neutral axis position and the curvature rate of the beam subjected to a bending moment were given in a coupled non-linear algebraic form that can be solved numerically. He later introduced a simplified analytical solution that can be used given that shift in neutral axis location and curvature rates from two different bend data are available [16,17].

In the present manuscript, four-point bending creep tests and compression tests were conducted on ZrB_2–20 vol% SiC at 1800 ℃. Most importantly, we showed the solution proposed by Chuang [17] to successfully predict the compressive stress exponent which we measured here. The predicted tensile creep parameters were within those published for refractory compounds under tension or tensile bending stress, and based on recent findings published by our research group. No experimental tensile data are available in the literature for direct comparison. In fact, for ZrB_2 composites, only flexure and compression experiments were carried out in the literature [7,18–23]. Additionally, we propose an enhanced specimen geometry for compression creep testing that allows higher creep strains to be reached prior to the onset of catastrophic specimen instability.

2 Experimental methods

2.1 Creep experiment

A complete description of the processing procedure of the materials used in the present manuscript is detailed in Section 2.1. of Ref. [18]. Both flexure and compression creep experiments were conducted in a clamshell furnace (DT-33-55, Deltchech, Inc., Denver, CO, USA) equipped with Molydisilicide heating elements capable of reaching 1900 ℃. For each experiment, the specimen was enclosed in a 7″ long vertical alumina tube with porous (90%) alumina refractory plugs at each end. Experiments were conducted under a flowing protective atmosphere

comprised of ultra-high-purity Argon (99.999%). During compression tests, displacements were measured using a video extensometer (Messphysik, Austria) capturing the movement of a marker (every 3 seconds) fixed on the SiC rod applied on top of the specimen. A dead load was supported by a weight applicator fixed on the SiC rod and equipped with water-cooled junctions. A grafoil sheet (Graftech Int. Lakewood, OH, USA) of less than 100 μm in thickness was introduced between the specimen and the SiC rod to prevent any undesired bonding between the rod and the specimen at high temperatures. Flexure specimens were subjected to four-point bending where the tensile outer-fiber displacement was captured using the video extensometer coupled with a custom built spring-loaded linear displacement dashpot and SiC extension probe rod contacting the tensile midpoint of each bar.

2. 2 Specimen geometry

Two sets of compression specimens were used in this study. A first set consisted of regular cubic specimens having the dimension of 3 mm × 3 mm × 3 mm. A second set comprised a new geometry that we propose, having the shape of the letter I (which we call I-shaped), with nominal height, length, and thickness (with reference to Fig. 1): $H_{max} = 7$ mm, $H_{min} = 3$ mm, $L_{max} = 7$ mm, $L_{min} = 3.5$ mm, and $T = 4$ mm. Notches on these specimens were made using a 1.2 mm diamond blade resulting in a radius of curvature of ~0.635 mm. The proposed new geometry is analogous to a Bridgman high pressure conical anvil where peak compressive stresses are localized to the web section preventing specimen/fixture deformation at the load contact areas. Unlike the conical anvil shape, machining the I-shaped geometry is relatively simple and it has several advantages.

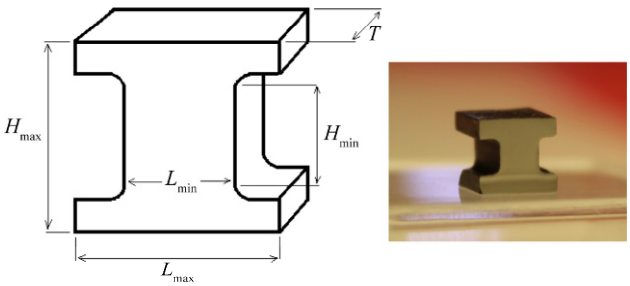

Fig. 1 I-shaped specimen dimensions (left). Snapshot of the specimen after 10% creep strain (right).

(1) The contact surface between the sample and the SiC rod is large compared to the section in the central rib of the specimen (middle part of height H_{min}), which reduces the stress applied on the rod, and hence the creep rate of the specimen and fixture contact area, while maintaining a higher stress on the specimen itself. As an illustration, for the particular dimensions considered here, if 30 MPa is applied on the center of the specimen, only 15 MPa is applied on the SiC rod reducing thus any contribution from SiC in the overall deformation and allowing for more accurate data to be collected. To prove this concept, a finite element model was implemented in Abaqus R0214a where an elastic I-shaped specimen is subject to a pressure of 15 MPa on one end and fixed on the other. The distribution of the stress component along the applied load direction shows that the compressive stress is localized along the central rib of the sample, major contributing part in the overall deformation (Fig. 2).

(2) It was also observed that this geometry reduces "barreling", commonly observed with cubic specimens after prolonged creep. In fact, interruption of several tests at different strain levels and observation of the specimens indicated that "barreling" was not noticeable in the I-shaped specimens below 10% strain, whereas less strains were allowed by the cubic samples. Strains were calculated based on the displacement δ captured by the extensometer and is equal to

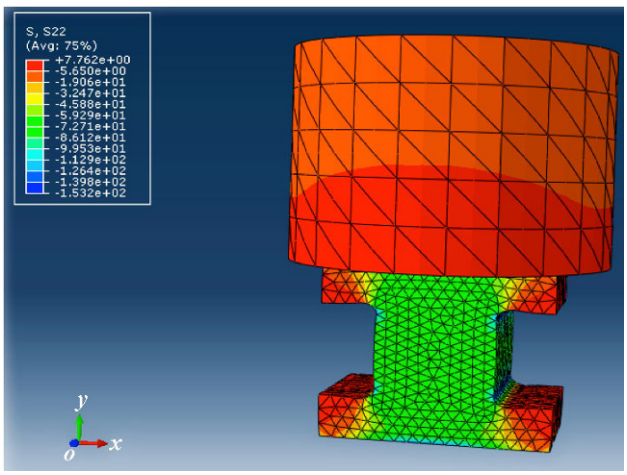

Fig. 2 Finite element model of the elastic I-shaped specimen subjet to unidirectional compression along its vertical axis. Effective part of the beam consists of the central rib with the highest compressive stress. Other parts of the specimen do not contribute to the overall strain and their effect can therefore be neglected.

$$\varepsilon = \frac{\delta}{H} \tag{3}$$

where the height H represents the effective height ($H_{\min}$) for the I-shaped specimens and is equal to the total height for the cubic samples. The outer-fiber strain of the flexure specimen (nominal dimension of 4 mm × 4 mm × 40 mm) was calculated from the tensile outer-fiber displacement δ based on linear elastic beam assumptions [7]:

$$\varepsilon = \frac{12h\delta}{3L^2 - 4a^2} \tag{4}$$

where h is the bar's height, L is the outer span, and a is the distance between the outer span and inner span.

3 Results

3. 1 Determination of neutral axis position in flexure specimens

Four-point bending results were used to calculate the neutral axis (NA) positions of two specimens that were subjected to two distinct bending moments. The compressive outer-fiber curvature of the deformed beam ρ_c was determined based on optical beam curvature measurements (Nikon Nis-Elements Documentation V3.22.00) fitted to a second order polynomial. Radius of curvatures R_c was then determined such that [24]:

$$\rho_c = ax^2 + bx + c \tag{5}$$

$$\frac{1}{R_c} = \left(\frac{d^2\rho_c}{dx^2}\right)\left[1 + \left(\frac{d\rho_c}{dx}\right)^2\right] \tag{6}$$

The neutral axis position h_c can be approximated as follows:

$$h_c = \frac{H_c}{H} = \frac{R_c}{H}\left(\frac{L}{\rho_c} - 1\right) \tag{7}$$

where H is the height of the beam and L is the length of the undeformed beam, equal as well to the length of the neutral axis (see Fig. 3). Results are summarized in Table 1.

Table 1 Four-point flexure measurements obtained at two different stresses

Test	Stress (MPa)	Load-point displacement rate (mm/s)	Neutral axis position	Normalized moment
1	20.3	7.33×10^{-4}	0.65	3.39
2	16.6	4.65×10^{-4}	0.64	2.77

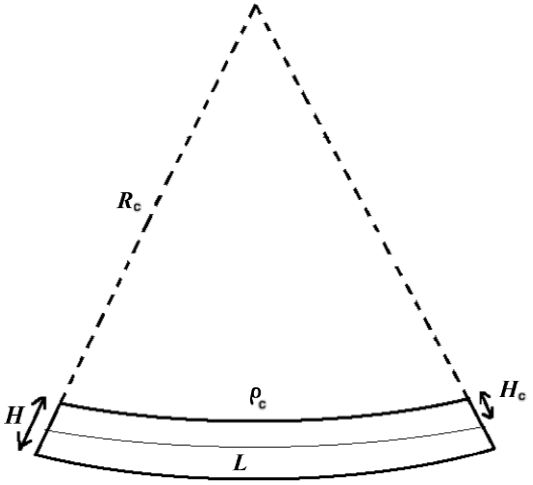

Fig. 3 Geometric parameters of the beam used to determine the neutral axis position (Eq. (7)) in four-point bending specimens.

3. 2 Creep curves

Compression creep experiments were conducted on both sets of specimens (regular cubic and I-shaped) at 1800 ℃ and stresses ranged between 10 and 40 MPa. Due to the transient nature of creep, particularly with the large accumulated strains observed here of ~10%, we extract the steady-state creep strain by non-linear regression fitting to each strain rate–strain creep curve following Luecke and Wiederhorn [25]:

$$\dot{\varepsilon} = \dot{\varepsilon}_s + \dot{\varepsilon}_p \exp\left(\frac{-\varepsilon}{\varepsilon_0}\right) \tag{8}$$

where $\dot{\varepsilon}_s$, $\dot{\varepsilon}_p$, and ε_0 represent, respectively, the steady-state creep rate, primary creep rate, and an initial strain constant. For each specimen, strains were determined by plotting the displacement captured by the extensometer over the initial height $H_{\min}$ for the I-shaped specimens and over the total height for the cubic specimens. Examples of creep curves at different stress levels are shown in Fig. 4, where higher strain rates correspond to higher stresses. In order to verify the reproducibility of the results, replicate experiments were conducted for each stress level. Pre-exponential coefficient A_c and stress exponent n_c of the Norton's power law equation (Eq. (2)) were obtained (Fig. 5) from a linear regression using the logarithm of Eq. (2).

An analysis of covariance for testing slope and intercept significance was conducted on both data obtained from the cubic specimens and the I-shaped specimens, yielding the two regression coefficients statistically indistinguishable. This, combined with the

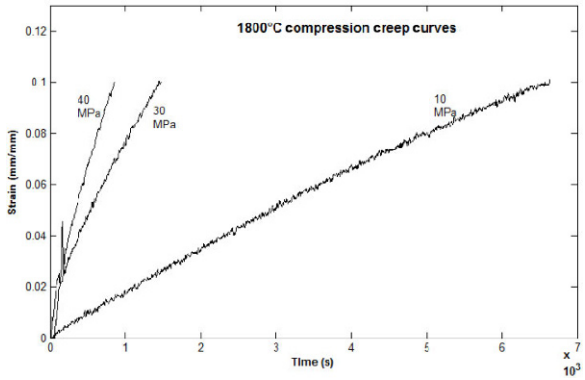

Fig. 4 Illustrative smoothed (moving average method) creep curves. Actual data were used in calculating the strain rates. Not all data were included for the clarity of the figure.

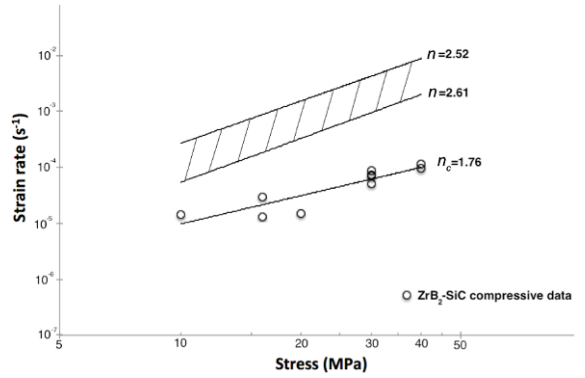

Fig. 5 Log–log plot of the compressive creep data for ZrB_2–20% SiC at 1800 ℃. Hatched region represents the predicted tensile region based on the "pinned" and predicted power law coefficients.

finite element results, validates and justifies the new proposed geometry. Therefore, data obtained from the two geometries will be treated equivalently in the rest of the manuscript. It should also be noted that although data obtained from the two sample sets are statistically similar, higher accuracy is definitely attributed to the I-shaped geometry as it allows the corresponding specimens to have higher deformation strains.

4 Discussion

The analytical analysis presented by Chuang was the first attempt to obtain Norton's power law constants (compressive and tensile) independently. The author avoided the numerical procedure initially presented in his original publication [15] by considering the neutral axis positions and curvature rates from two separate creep tests, offering thereby closed form solutions to all the parameters [16]. Derivations of Eqs. (9)–(13) are detailed in Refs. [16,17] and are not presented here. In the case where inequality (9) is verified, solutions (9) to (12) apply [17]:

$$\frac{n_t+1}{2n_t+1} \gg \frac{(2n_t+1)(n_c+1)-(2n_c+1)(n_t+1)}{h_c(2n_c+1)(2n_t+1)} \tag{9}$$

For the range of values expected for n_t in the present system, and after inspection of different parameters, inequality (9) can be accepted for the present system and Chuang's equations can be adopted [17]:

$$n_c = \frac{Ln\dfrac{\dot{k}_1}{\dot{k}_2}\dfrac{h_{c1}}{h_{c2}}}{Ln\dfrac{m_1}{m_2}\dfrac{h_{c2}}{h_{c1}}} \tag{10}$$

$$n_t = \frac{Ln\dfrac{\dot{k}_1}{\dot{k}_2}\dfrac{h_{t1}}{h_{t2}}}{Ln\dfrac{m_1}{m_2}\dfrac{h_{t2}}{h_{t1}}} \tag{11}$$

$$A_c = \frac{\dot{k}\left(\dfrac{n_c}{1+n_c}\right)^{n_c}(h_c)^{1+n_c}}{\left[\dfrac{m(1+2n_t)}{1+n_t}\right]^{n_c}} \tag{12}$$

and

$$A_t = \frac{\dot{k}\left(\dfrac{n_t}{1+n_t}\right)^{n_t}(h_t)^{1+n_t}}{\left[\dfrac{m(1+2n_t)}{1+n_t}\right]^{n_t}} \tag{13}$$

$\dot{k}$, h, and m are the load-point displacement rate, neutral axis position, and normalized applied moment, respectively. Subscripts 1 and 2 refer to test number and subscripts c and t, as above, indicate compression and tension constants respectively.

The compressive stress exponent calculated from Eq. (10) agrees well with the measured values (Table 2) 1.85 and 1.76, respectively. Wider error was expected for the pre-exponential factor, A_c, due to (i) contribution from the stress exponent error from Eq. (10) used in Eq. (12) and (ii) use of load-point displacement rates instead of curvature rates leading to a systematic error of ~20% as stated in Ref. [17]. Although the calculated results were satisfactory, compressive creep data were included to determine the tensile parameters by "pinning" the theoretical values to the experimental measurements by adjusting the

neutral axis position ratio h_{c1}/h_{c2}. The difference obtained between the calculated and experimental compression data can be regarded as an error that will induce through the calculation method to the tensile results. Thus, it can be reasonably assumed that the difference between the calculated and adjusted (by pinning) tensile stress exponents will delimit some error range, where tensile data points are predicted to fall into (hatched area in Fig. 5). Table 2 includes the numerical values for the different power law parameters.

A compressive stress exponent of $1< n_c < 2$ suggests diffusion creep, although grain boundary sliding may operate as parallel deformation mechanism. Nabarro [26], Herring [27] (or Nabarro–Herring), and Coble [28] models predict a stress exponent of unity for lattice and grain boundary diffusion mechanisms, respectively, with different grain size dependence. Harper–Dorn creep [29] also exhibits a linear strain rate–stress dependence and is more likely to operate in coarse-grained polycrystalline materials under very low stresses with no grain size dependence [30]. In the case where grain boundary sliding dominates, vacancy diffusion accommodates the sliding event with minimum contribution to the deformation rate. In this context, Ashby and Verrall [31] developed a model involving grain switching positions with neighbors with no grain shape change. Raj and Ashby [32] considered several symmetric grain boundary protrusions and predicted a stress exponent of 1 as well. When grain boundary sliding, accommodated by dislocation motion, is rate limiting, a stress exponent of 2 is predicted. Ball and Hutchison [33] considered the situation where dislocations glide through unfavorably oriented grains, pile-up at grain boundaries and subsequently climb through and along boundaries. Gifkins [34] presented a similar mechanism with the exception that dislocation activity occurs in the grain boundary region called “mantle” where grain boundary dislocations pile-up at the triple edge and climb to the adjacent grain mantle to permit sliding and grain rotations.

Table 2 Power law parameters determined experimentally and using Chuang [17]

	Pre-exponential coefficient A (s^{-1})	Stress exponent n
Compression (experimental)	1.63×10^{-7}	1.76
Compression (predicted)	6.27×10^{-7}	1.85
Tension (predicted)	8.12×10^{-7}	2.52
Tension (adjusted)	1.33×10^{-7}	2.61

Recent research [22,23], conducted in our group, on ZrB_2–20% SiC creep behavior at 1800 ℃ has shown geometrically necessary dislocation activity increases within grain boundary networks to accommodate the grain boundary sliding event during high temperature deformation. The creep mechanism was supported by direct observation of the microstructure where a series of nano-indents were placed on a polished surface and tracked after the deformation. Grain boundary sliding was manifested as grain rotations and translations. Additionally, quantification of geometrically necessary dislocations using electron back scatter diffraction techniques revealed increased activity near the grain boundaries to achieve the necessary accommodation for the sliding grains [22,23]. Presence of limited cavitation in the compressive microstructures indicates grain boundary sliding mechanism operating in the present specimens. Limited cavities were similarly present in the compressive side of the flexure specimens (Fig. 6) [18]. Cavity formation may indicate accommodation in cooperation with the mantle mechanism, in response to grain boundary sliding in compression. Furthermore, the stress exponent suggests further contribution from an independent diffusional creep mechanism in pure compression. Therefore, we expect grain boundary sliding and diffusional creep to dominate the deformation in compression creep of ZrB_2–20% SiC at 1800 ℃, consistent with the flexure findings [22,23]. The dislocation accommodated sliding attributed to the present material should hold for both compressive and tensile components of the deformation as tensile and compressive regions in four-point bending samples did not show substantial microstructural differences at 1800 ℃ with higher cavitation observed along the tensile surface [18]. Consequently, under pure tension, the tensile stress exponent of $n_t > 2$, implies increased contribution from an independent cavitation mechanism [18,22,23].

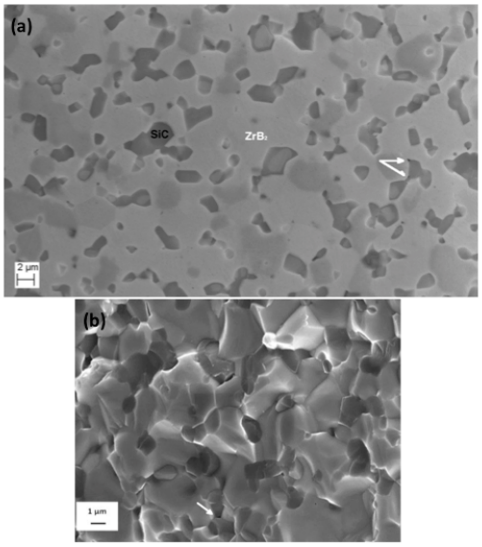

Fig. 6 Scanning electron micrographs depicted from the center region of a compression specimen after ~8% strain showing continuous microstructure with the formation of few cavities (white arrows) (a). Similar cavities were observed within the compressive region in flexure specimens (b). Samples corresponding to (a) and (b) were subjected to similar conditions of stress (~20 MPa) and temperature (1800 ℃).

5 Conclusions

The analytical solution proposed by Chuang coupled with our compression and flexure data were used to determine the tensile power law creep constants for ZrB_2–20 vol% SiC composite at 1800 ℃. The new geometry used in compression tests showed similar strain rates as the cubic specimens but allowed for higher strains to be reached. Excellent agreement in the prediction of the compressive stress exponent was found between the analytical method and the experimental data. A tensile stress exponent of 2.61 is to be expected. Based on the determined stress exponents and comparisons with our recent findings [18,22,23], grain boundary sliding accommodated by "mantle" dislocations combined with diffusional processes control the compressive creep behavior of ZrB_2–20% SiC at 1800 ℃. Similar grain boundary sliding mechanism enhanced by a cavitation mechanism should operate in pure tension.

Acknowledgements

The authors gratefully acknowledge AFOSR program monitor Ali Sayir, under grant # FA9550-09-1-0200, for partial support of this work. Extended appreciation goes to Dr. Pradeep Sharma for insightful comments that greatly improved this manuscript and Dr. Bill Fahrenholtz, Dr. Greg Hilmas, and Mr. Eric Neuman at the Missouri University of Science and Technology, Rolla, MO, USA, for providing the materials used in this study.

References

[1] Fahrenholtz WG, Hilmas GE, Talmy IG, *et al*. Refractory diborides of zirconium and hafnium. *J Am Ceram Soc* 2007, **90**: 1347–1364.

[2] Chamberlain AL, Fahrenholtz WG, Hilmas GE, *et al*. High-strength zirconium diboride-based ceramics. *J Am Ceram Soc* 2004, **87**: 1170–1172.

[3] Guo S-Q. Densification of ZrB_2-based composites and their mechanical and physical properties: A review. *J Eur Ceram Soc* 2009, **29**: 995–1011.

[4] Levine SR, Opila EJ, Halbig MC, *et al*. Evaluation of ultra-high temperature ceramics for aeropropulsion use. *J Eur Ceram Soc* 2002, **22**: 2757–2767.

[5] Squire TH, Marschall J. Material property requirements for analysis and design of UHTC components in hypersonic applications. *J Eur Ceram Soc* 2010, **30**: 2239–2251.

[6] Monteverde F, Bellosi A, Scatteia L. Processing and properties of ultrahigh temperature ceramics for space applications. *Mat Sci Eng A* 2008, **485**: 415–421.

[7] Talmy IG, Zaykoski JA, Martin CA. Flexural creep deformation of ZrB_2/SiC ceramics in oxidizing atmosphere. *J Am Ceram Soc* 2008, **91**: 1441–1447.

[8] Tandon R, Dumm HP, Corral EL, *et al*. Ultra high temperature ceramics for hypersonic vehicle applications. SAND2006-2925. Sandia National Laboratories, 2006.

[9] Norton FH. *The Creep of Steel at High Temperatures*. New York: McGraw-Hill Book Company, Inc., 1929.

[10] Yoon KJ, Wiederhorn SM, Luecke WE. Comparison of tensile and compressive creep behavior in silicon nitride. *J Am Ceram Soc* 2000, **83**: 2017–2022.

[11] Lange FF. Non-elastic deformation of polycrystals with a liquid boundary phase. In: *Deformation of Ceramic Materials*. Bradt RC, Tressler RE, Eds. Boston, MA, USA: Springer, 1975: 361–381.

[12] Finnie I. Method for predicting creep in tension and compression from bending tests. *J Am Ceram Soc* 1966, **49**: 218–220.

[13] Talty PK, Dirks RA. Determination of tensile and compressive creep behavior of ceramic materials from bend tests. *J Mater Sci* 1978, **13**: 580–586.

[14] Xu BX, Yue ZF, Eggeler G. A numerical procedure for retrieving material creep properties from bending creep tests. *Acta Mater* 2007, **55**: 6275–6283.

[15] Chuang T-J. Estimation of power-law creep parameters from bend test data. *J Mater Sci* 1986, **21**: 165–175.

[16] Chen C-F, Chuang T-J. Improved analysis for flexural creep with application to SiAlON ceramics. *J Am Ceram*

Soc 1990, **73**: 2366–2373.
[17] Chuang T-J. Some remarks on "Improved analysis for flexural creep with application to SiAlON ceramics". *J Am Ceram Soc* 1998, **81**: 2749–2750.
[18] Bird MW, Aune RP, Yu F, *et al*. Creep behavior of a zirconium diboride–silicon carbide composite. *J Eur Ceram Soc* 2013, **33**: 2407–2420.
[19] Kats SM, Ordan'yan SS, Unrod VI. Compressive creep of alloys of the $ZrC–ZrB_2$ and $TiC–TiB_2$ systems. *Powder Metall Met Ceram* 1981, **20**: 886–890.
[20] Spivak II, Andrievskii RA, Klimenko VV, *et al*. Creep in the binary systems $TiB_2–TiC$ and $ZrB_2–ZrN$. *Powder Metall Met Ceram* 1974, **13**: 617–621.
[21] Bird MW, Aune RP, Thomas AF, *et al*. Temperature-dependent mechanical and long crack behavior of zirconium diboride–silicon carbide composite. *J Eur Ceram Soc* 2012, **32**: 3453–3462.
[22] Bird MW, Becher PB, White KW. Grain rotation and translation contribute substantially to flexure creep of a zirconium diboride silicon carbide composite. *Acta Mater* 2015, **89**: 73–87.
[23] Bird MW, Rampton T, Fullwood D, *et al*. Local dislocation creep accommodation of a zirconium diboride silicon carbide composite. *Acta Mater* 2015, **84**: 359–367.
[24] Jakus K, Wiederhorn SM. Creep deformation of ceramics in four point bending. *J Am Ceram Soc* 1988, **71**: 832–836.
[25] Luecke WE, Wiederhorn SM. A new model for tensile creep of silicon nitride. *J Am Ceram Soc* 1999, **82**: 2769–2778.
[26] Nabarro FRN. Deformation of crystals by the motion of single ions. Report of a conference on the strength of solids. London: Physical Society, 1948: 75–90.
[27] Herring C. Diffusional viscosity of a polycrystalline solid. *J Appl Phys* 1950, **21**: 437–445.
[28] Coble RL. A model for boundary diffusion controlled creep in polycrystalline materials. *J Appl Phys* 1963, **34**: 1679–1682.
[29] Kumar P, Kassner ME, Langdon TG. Fifty years of Harper–Dorn creep: A viable creep mechanism or a Californian artifact? *J Mater Sci* 2007, **42**: 409–420.
[30] Mohamed FA, Langdon TG. Deformation mechanism maps based on grain size. *Metall Mater Trans B* 1974, **5**: 2339–2345.
[31] Ashby MF, Verrall RA. Diffusion-accommodated flow and superplasticity. *Acta Metall* 1973, **21**: 149–163.
[32] Raj R, Ashby MF. On grain boundary sliding and diffusional creep. *Metall Trans* 1971, **2**: 1113–1127.
[33] Ball A, Hutchison MM. Superplasticity in the aluminium–zinc eutectoid. *Mater Sci Tech* 1969, **3**: 1–7.
[34] Gifkins RC. Grain-boundary sliding and its accommodation during creep and superplasticity. *Metall Trans A* 1976, **7**: 1225–1232.